

Competition between d -wave superconductivity and magnetism in uniaxially strained Sr_2RuO_4

Jonas B. Profe,^{1,2} Sophie Beck,² Dante M. Kennes,^{1,3} Antoine Georges,^{4,2,5,6} and Olivier Gingras²

¹*Institute for Theoretical Solid State Physics, RWTH Aachen University and JARA Fundamentals of Future Information Technology, 52062 Aachen, Germany*

²*Center for Computational Quantum Physics, Flatiron Institute, 162 Fifth Avenue, New York, New York 10010, USA*

³*Max Planck Institute for the Structure and Dynamics of Matter and Center Free-Electron Laser Science, Hamburg, Germany*

⁴*Collège de France, Université PSL, 11 place Marcelin Berthelot, 75005 Paris, France*

⁵*Centre de Physique Théorique, Ecole Polytechnique, CNRS, Institut Polytechnique de Paris, 91128 Palaiseau Cedex, France*

⁶*DQMP, Université de Genève, 24 quai Ernest Ansermet, CH-1211 Genève, Suisse*

(Dated: August 1, 2024)

The pairing symmetry of Sr_2RuO_4 is a long-standing fundamental question in the physics of superconducting materials with strong electronic correlations. We use the functional renormalization group to investigate the behavior of superconductivity under uniaxial strain in a two-dimensional realistic model of Sr_2RuO_4 obtained with density functional theory and incorporating the effect of spin-orbit coupling. We find a dominant $d_{x^2-y^2}$ superconductor mostly hosted by the d_{xy} -orbital, with no other closely competing superconducting state. Within this framework we reproduce the experimentally observed enhancement of the critical temperature under strain and propose a simple mechanism driven by the density of states to explain our findings. We also investigate the competition between superconductivity and spin-density wave ordering as a function of interaction strength. By comparing theory and experiment, we discuss constraints on a possible degenerate partner of the $d_{x^2-y^2}$ superconducting state.

INTRODUCTION

Almost 30 years after the discovery of superconductivity in Sr_2RuO_4 (SRO) [1], the symmetry of its superconducting order parameter (SCOP) remains an open question. Initially, its similarities with $^3\text{Helium}$ made it a prime candidate for spin-triplet pairing [2], corroborated by various measurements [3–11]. Along with observations of time-reversal symmetry breaking (TRSB) supporting a two-component order parameter [12, 13], the superconducting (SC) state was believed for a long time to be a chiral p-wave spin-triplet. However, conflicting evidence presented in various studies remained to be explained [14, 15]. First, the presence of nodal excitations is unexpected in a chiral p-wave SC [16–19]. Second, the low critical field H_{c2} exhibited by SRO is typical for Pauli-limited spin-singlet SC [20] and the transition into the normal state upon applying a magnetic field appears to be first-order [21, 22], with indications of a Fulde-Ferrell-Larkin-Ovchinnikov state for a certain parameter range, strongly pointing to a singlet SCOP [23]. Third, none of the topologically protected edge states predicted in chiral p-wave states were observed in experiments [24–27], although this could be explained by a high Chern number [28].

In recent years, the chiral p-wave picture has basically been dismissed. First, the careful replications of key nuclear magnetic resonance experiments previously interpreted as supporting spin-triplet pairing have highlighted a heating effect and instead concluded that the SCOP corresponds to spin-singlet pairs [29–31]. Second, applying uniaxial strain along the x principal crystallo-

graphic axis was found to enhance the critical temperature (T_c) [32, 33] and to lower the Fermi liquid coherence scale [34]. This enhancement was shown to be maximal where the FS undergoes a Lifshitz transition, corresponding to a van Hove singularity (vHs) in the density of states (DOS), at a time-reversal invariant momentum point, inconsistent with odd-parity SCOPs like p-wave [35]. Nowadays, a consensus appears to be crystallizing around the spin-singlet and even-parity natures of the SCOP, yet the debate is still ongoing. While ultrasounds experiments support the conclusion of a two-component order parameter [36, 37] inferred by the observation of TRSB and the splitting between T_c and the TRSB transition temperature [38, 39], there are no two-temperature signature in bulk thermodynamical experiments such as specific heat and elastocalorimetry as well as scanning SQUID microscopy [40–43]. As a result of this plethora of experimental evidence, SRO can be seen both as a critical playground for testing new theories with the goal of potentially unifying some of these contradicting observations and as a testbed to verify whether our interpretations of specific experiments are valid. Either way, it constitutes an ideal system to considerably advance our understanding of the mechanisms for unconventional superconductivity [44].

Many theoretical proposals have been put forward as potential SCOPs. Initially classified as a chiral p-wave [45–52], the recent experimental evidence motivated further proposals, including two-dimensional states such as $s + id_{xy}$ [53–56], $d_{x^2-y^2} + ig_{xy(x^2-y^2)}$ [56–61], a combination of even and odd-parity irreducible representations (irreps) [62], inter-orbital pairing [63, 64], $d+d$ [65],

and $d_{x^2-y^2}$ (plus odd-frequency) [66–69]. Some three-dimensional states were also proposed, for example E_g $d_{yz} + id_{zx}$ [70, 71] and helical $p_x + p_y$ [72].

A general overview of possible ordering states in terms of their irreducible representations is given in Ref. 63, 73.

In this paper, we investigate the leading superconducting instabilities of SRO using functional renormalization group (FRG) calculations [74], applied to a realistic model of the electronic structure derived from density functional theory (DFT) [75] that includes spin-orbit coupling (SOC). Note that previous studies of SRO using FRG were performed on tight-binding models, fitted to photoemission spectroscopy measurements [46, 48, 59, 76–78]. In order to compare to experiments, we study the effect of uniaxial strain, tracking the evolution of T_c as well as the type of ordering. We find a phase diagram with two different magnetic orders that compete with a single SCOP transforming like the B_{1g} irrep (often labelled as $d_{x^2-y^2}$ -wave). This competition is found to depend sensitively on the choice of interaction parameters. We show that a proper range of parameters lead to an increase of the superconducting T_c in good agreement with experiments.

RESULTS

Electronic structure. — To describe the low energy electronic structure of SRO for the different strain values, we perform *ab initio* DFT calculations downfolded onto the t_{2g} orbitals of the ruthenium atoms using maximally localized Wannier functions as detailed in the methods section. There is an extensive literature using tight-binding Hamiltonians from *ab-initio* electronic structure calculations based on DFT for SRO, presenting overall very consistent results at the DFT level. Beyond DFT, it was shown that replacing the local SOC parameter of 100 meV obtained with DFT with a value twice as large $\lambda_{\text{SOC}} \simeq 200$ meV yielded a considerably better agreement with the experimentally observed Fermi surface [79], in consistent with the correlation-induced enhancement predicted theoretically [80, 81]. Indeed, this parameter adjustment leads to improved agreement with the FS both in the unstrained case and with the experimentally observed critical strain [79–86]. A comparison to a selection of previously published tight-binding models is shown in App. A. Note that the addition of SOC breaks the $SU(2)$ spin symmetry, but preserves an orbitally dependent $SU(2)$ (so called pseudospin) symmetry [68]. We keep the SOC fixed for all strain values [87].

In order to account for strong electronic correlations in this multi-orbital system, we use for most parts of this paper the $O(3)$ symmetric Hubbard-Kanamori parametrization of the interaction Hamiltonian [88], which involves two key energy scales: the on-site Hubbard repulsion U and the Hund coupling J - see methods. As done routinely in FRG calculations [46, 48, 76–78, 89–100], we neglect the flow of the self-energy in our calcu-

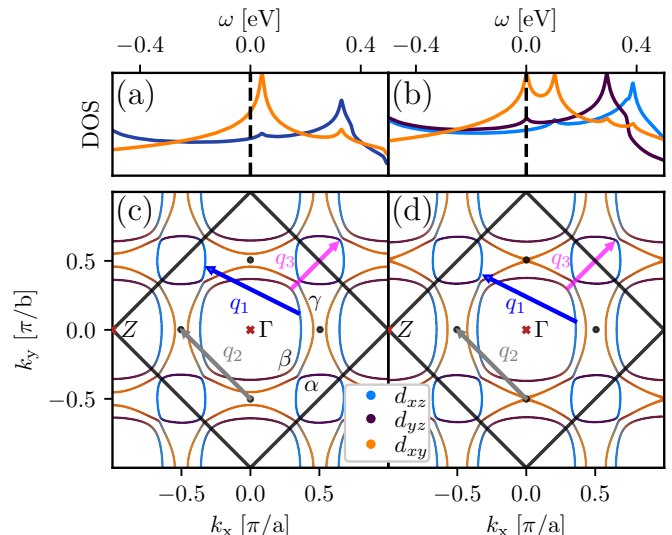


FIG. 1. **Partial density of states and Fermi surface for the three t_{2g} orbitals** of the unstrained (left) and the optimally strained (right) systems in the upper and lower panels respectively. The optimal strain of 0.8% corresponds to the system being closest to the Lifshitz transition. Here, a (b) is the lattice parameter in the x (y) direction, with $a = b$ in the $\epsilon_{xx} = 0$ case. The black dots indicate the position of the vHs of the d_{xy} orbital. The three dominant spin-density wave ordering vectors q_1 , q_2 and q_3 are highlighted in black, gray and pink, respectively. The first Brillouin zone is marked by a black square. We mark the Γ and Z point by red crosses. Furthermore, we labeled the α , β and γ sheets on the FS for $\epsilon_{xx} = 0$. In the unstrained case, the partial DOS for the d_{xz} and d_{yz} orbitals is identical, which is emphasized by the color mixing.

lations. Hence, the interaction parameters (U, J) should be considered as effective interactions with significance within our FRG framework rather than having a first-principle meaning. In this perspective, it is important to explore how the various instabilities are tuned by varying the interaction parameters. The guiding principles for constructing the model utilized follow two rules

- We start from state of the art DFT with added spin-orbit coupling λ_{SOC} such that we do have the right Fermi surface.
- The choice of our interaction parameters is restricted in such a manner that, from the Wannier model defined above, we recover the correct peak positions of the interacting spin-spin susceptibility as measured in experiments.

The FS and the density of states (DOS) obtained from this downfolded t_{2g} model are displayed on Fig. 1. The left column corresponds to the unstrained system ($\epsilon_{xx} = 0$) and the right columns to the optimally uniaxially strained system for which the Fermi level is at the vHs ($\epsilon_{xx} = \epsilon_{xx}^{\text{vHs}}$). Note that $\epsilon_{xx}^{\text{vHs}}$ does not include quasi-particle renormalization and therefore is not the same

value as in experiments. The D_{4h} space group symmetry of the unstrained system is lowered down to D_{2h} by uniaxial strain and the B_{1g} irreducible representation of D_{4h} , of greatest relevance to our study, turns into the A_g irreducible representation of D_{2h} .

Note the slightly unusual presentation of the FS in Fig. 1: this is due to the transformation from a tetragonal basis into a x - y plane which has to be done in this fashion to ensure periodicity of the downfolded model in the two-dimensional primitive cell. Due to this, we have not a single but two k_z values in the first primitive cell, i.e. the Z -point is located at the corner of the black square. All the results that follow are obtained for the quasi-2D model restricted to $k_z = 0$ and $k_z = 2\pi/c$, shown on Fig. 1. We verify that they are agreeing with the results from full 3D calculations in App. F.

The lowering of the symmetry under uniaxial strain lifts the degeneracy between the d_{xz} and the d_{yz} orbitals of the ruthenium atom, as seen in the DOS in Fig. 1. It also splits the d_{xy} van-Hove singularity into two parts: one drifting away from the FS (x -direction) and one drifting towards the FS and crosses it at the Lifshitz transition ($\epsilon_{xx}^{vHs} \sim 0.8\%$ strain). On the FS shown in Fig. 1, we also highlight the dominant nesting vectors of the bare particle-hole susceptibility (χ_{PH}^0), see App. B. First, $q_1 = (2\pi(3a)^{-1}, \pi(3b)^{-1})$ (and all those related by symmetry) connects the α and β sheets of the FS. Second, $q_2 = (\pi(2a)^{-1}, \pi(2b)^{-1})$ is connecting two van-Hove singularities and should become relevant at large interactions. Third, $q_3 = (\pi(3a)^{-1}, \pi(3a)^{-1})$ also connects the α and β sheet of the FS. These vectors are consistent with the dominant spin fluctuations observed in neutron scattering experiments [101, 102]. Note that there is a family of nesting vectors connecting α and β sheet, all close to q_1 .

With these insights from the non-interacting FS and DOS in mind, we proceed with the phase diagrams as a function of U and J for the unstrained and the $\epsilon_{xx} = \epsilon_{xx}^{vHs}$ cases. The results are presented on Fig. 2. The background color corresponds to the energy scale Λ_c (expressed in meV) at which a divergence of the corresponding coupling is observed. The fastest divergent coupling corresponds to the dominant instability, which can either be superconductivity (in which case Λ_c is expected to be proportional to the Berezinskii-Kosterlitz-Thouless [103–105] critical temperature T_{BKT}) or a spin-density wave (SDW) (in which case Λ_c can be interpreted as the characteristic scale associated with the growth of the correlation length) [106]

At the lowest U and J values, we find no divergence down to the lowest energy scale resolvable with our momentum resolution, and thus conclude that the system remains in the Fermi liquid (FL) state down to that scale. Apart from this unique point, we find three types of instabilities. Up to moderate U and low but finite J , we find a $d_{x^2-y^2}$ superconducting instability (corresponding to B_{1g} symmetry for the unstrained system, turning into A_g for the strained one). Upon increasing U or J , we

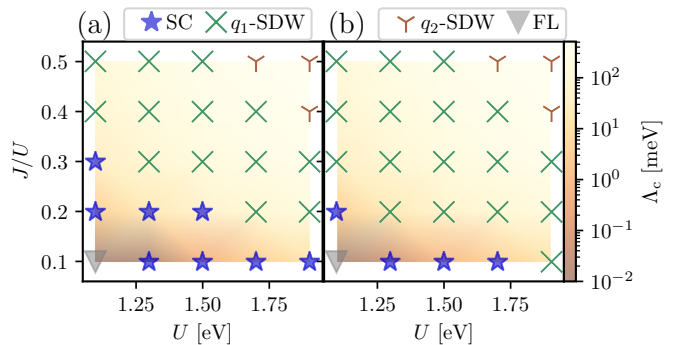


FIG. 2. **Phase diagrams in the U - J parameter space** for the unstrained (a) and the optimally strained (b) systems. The background color indicates the critical scale Λ_c , proportional to the ordering energy scale, with the corresponding color bar on the right. The phases are either a B_{1g} superconductor (A_g under uniaxial strain), two different spin-density waves (SDWs) or a Fermi-liquid (FL). The q -vectors associated to the SDWs are shown in Fig. 1.

find that the dominant instability becomes a SDW with ordering vector q_1 . At even larger U and J , the system undergoes a high-temperature transition to another SDW phase characterized by the ordering vector q_2 . These ordering vectors are visible in both non-interacting and interacting susceptibilities. Since we do not incorporate the effect of the self-energy, we cannot observe the shift of the q_3 peak observed in Ref. [55].

Phase diagram and magnetic orderings. — The q_1 -SDW is driven by strong nesting between the α and β sheets. A corresponding peak in the spin-spin susceptibility has been well discussed both in the context of experimental observations [6, 107] and theoretical discussions [54, 67]. It should be noted that this vector is connecting two different values of k_z when backfolded in the three dimensional Brillouin zone. Its in plane analog, $q_3 = (\pi(3a)^{-1}, \pi(3a)^{-1})$, was found to be subleading in earlier three-dimensional studies using the random phase approximation (RPA) [54]. The q_3 peak is also found in DMFT calculations including vertex corrections [55, 108]. Here, we find the q_1 ordering to be the leading one, with the q_3 ordering also diverging but with smaller absolute magnitude. The increase of Λ_c can be understood in terms of the Stoner criterion being fulfilled at a larger scale for larger U or J . At higher energy scales, the vHs are strongly smeared. This effect increases the importance of the q_2 ordering vector connecting two vHs points, leading to the emergence of the q_2 -SDW phase.

When applying uniaxial strain, the parameter range where we find a SDW is increased. This can be understood from the increase of the DOS at the Fermi level, which leads to a larger χ_{PH}^0 and thereby a smaller interaction is required to fulfill the Stoner criterion. Beyond this effect, straining does not affect the structures of the phases and the q_2 -phase is still observable in the same parameter region, as the changes of the FS due to strain have counteracting effects: while in the y -direction the

FS touches the vHs, it drifts further away from it in the x -direction.

Note that as we increase the strain beyond the Lifshitz transition, we do not find the SDW that is observed in experiments [38, 41]. The emergence of this phase has been understood as the removal of all curvature of the γ sheet between the upper/lower vHs and the X/X' points, which leads to strong nesting along this direction [109]. We do not observe this phase at any investigated strain value. As was pointed out in Ref [110], strain suppresses quantum fluctuations preventing the ordered magnetic state, such that at high strain the phase transition emerges. Therefore, observing this transition in a diagrammatically unbiased approach is currently out of reach numerically, as it would require a full inclusion of the frequency dependence as well as multi-loop contributions [111]. We hope to overcome this shortcoming in the future.

Superconductivity. — In the following, the superconducting phase is analyzed using a linearized gap equation on the FS. As shown in Fig. 3, we find a gap that transforms according to a B_{1g} for $\epsilon_{xx} = 0$ (A_g for $\epsilon_{xx} = \epsilon_{xx}^{\text{vHs}}$) representation of the D_{4h} (D_{2h}) point groups. In the band basis, this state has a dominant overlap with the $d_{x^2-y^2}$ harmonic and its main weight stems from the d_{xy} orbital. Such a type of superconductor has been observed in several other studies [53, 54, 58, 59, 66–68, 109, 112]. Although spin-orbit mixing distributes pairing over the different FS sheets, the dominant d_{xy} orbital character that we find does lead to a larger pairing on the γ sheet. It should be noted however that experiments indicate that the gap function is sizeable on all three Fermi surface sheets. This potential difficulty could be resolved by employing an analysis based on the combination of FRG and mean-field theory [113].

The spectrum of the pair-pair susceptibility at Λ_c contains the information of all possible subleading SCOPs. By analyzing this spectral distribution, we find a clear separation of the eigenvalue of the $d_{x^2-y^2}$ superconducting state by at least one order of magnitude from all eigenvalues of other SCOPs, for all parameters investigated. While this excludes any immediate degenerate state, no statement about the proximity of different symmetry states or individual critical temperatures can be drawn from FRG, because within this method the dominant instability is signalled by a divergent coupling and susceptibility [114]. However, from the hierarchy standpoint, we still can extract tendencies towards different orderings as discussed in App. E. This hierarchy reveals that the p-wave pairing state [46, 48, 78] is always clearly subleading by a large margin and both extended s-wave and g-wave are consistently closer to the d-wave. We simulate the full 3D model at a selected point to check for consistency of our 2D simulations. The results of these 3D simulations are shown in App. F and agree with the 2D results.

The superconducting phase is generated by a spin-fluctuation mechanism. The couplings U and J are cru-

cial tuning knobs determining the onset of the phase and also control the transition to the neighbouring magnetic phase. When increasing U , the transition to a SDW is understood from the underlying ladder-type diagrams diverging as soon as U becomes larger than the critical value. Below that critical U , the still strong spin-fluctuations can drive a superconducting instability. However, increasing J has a more complex effect since it affects two different physical processes, which we discuss in terms of two distinct couplings, J_{ss} and J_{dd} in Eq. (1). J_{ss} promotes spin-flip and pair-hopping processes, thus reducing the tendency to order magnetically while also increasing pair-correlations. J_{dd} decreases inter-orbital density-density interactions, which reduces the inter-orbital repulsion between electrons on the same site. We unravel which of the two effects is most relevant for a) superconductivity and b) the magnetic transition. This is achieved by varying the two quantities independently, first in a simple RPA calculation and then in a full FRG calculation.

For the simple RPA calculation, we calculate χ_{PH}^0 at $\Lambda = 11.6$ meV. We chose $U = 0.3$ eV to circumvent the Stoner instability and vary J_{ss} and J_{dd} between $0.0U$ and $0.3U$ independently. The dominant components of the bare susceptibility are presented in Fig. 8 of App. D. In general, we observe that varying J_{ss} has barely any effect on $\chi_{\text{PH}}^{\text{RPA}}$. J_{dd} , on the other hand, increases the inter-orbital components by a significant amount. Therefore we expect J_{ss} to have a weaker impact on the superconducting transition. Physically this is expected since J_{ss} hampers the spin-fluctuations which are required to obtain an effective attraction required by the superconducting state. To support this claim and understand better the underlying interference mechanism, we developed a simple 2-band toy model in App. D.

In the full FRG simulation, we verify these conclusions, i.e. increasing J_{ss} leads to a transition only at much larger values than the one for J_{dd} . See Fig. 9 of App. D. Interestingly, J_{ss} will generate a stronger admixture of higher order angular momentum superconductivity hosted by the d_{yz} and d_{zx} orbitals. These are however still sub-leading to the $d_{x^2-y^2}$ superconducting state.

Influence of strain. — Finally, we compare our results with experiments. We do so by examining the effect of strain from $\epsilon_{xx} = 0.0\%$ to $\epsilon_{xx} = 1.3\%$ on the leading instability of different (U, J) combinations. The general behavior of T_c is consistent with earlier studies [76, 109, 115], while the predicted phases partially differ. The different critical scales Λ_c can be interpreted as an estimate for T_c of the instability. The results for all superconducting data points are summarized in Fig. 4.

For systems that start with a large initial critical scale at zero strain ($\Lambda_c(\epsilon_{xx} = 0)$), no significant enhancement with respect to strain is found. The enhancement of T_c is much larger when $\Lambda_c(\epsilon_{xx} = 0)$ is smaller. This effect can be understood by looking at the DOS: large energy scales, or large temperatures, correspond to smeared out features in the DOS. Thus, the shift of the vHs due to

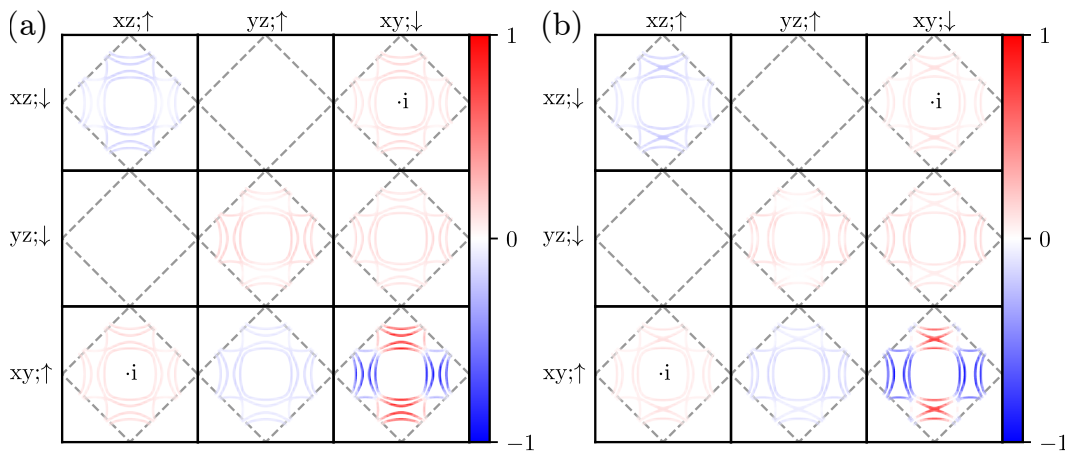


FIG. 3. **Example of superconducting order parameters** found in Fig. 2, calculated from a linearized gap equation in orbital space. They correspond to $U = 1.1$ eV and $J = 0.22 U$. The 3×3 matrices represent the spin-orbital states of the paired electrons in the inter-pseudospin channel since the intra-pseudospin terms are vanishing. Each panel shows the momentum structure. We present in panel (a) and (b) the unstrained case with $\epsilon_{xx} = 0$ and the optimally strained case with $\epsilon_{xx}^{\text{vHs}}$ respectively. The SCOP transforms like the one-component B_{1g} (A_g) irreducible representation of the D_{4h} (D_{2h}) group which requires some components to be purely imaginary due to the transformation behavior of the spin-orbitals under rotational symmetries [68]. Since the gap function is only known up to a prefactor, we rescale it from -1 to 1 , the sign and value is encoded in the colorbar. The first Brillouin-zone is marked by the grey square.

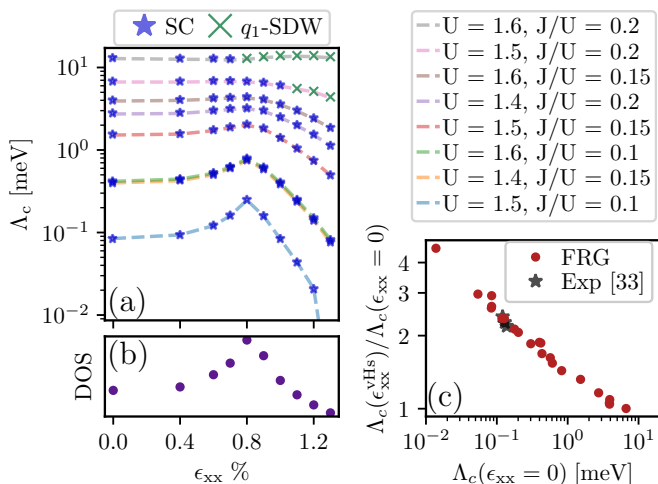


FIG. 4. **Effect of strain ϵ_{xx} on the critical scale Λ_c** for different values of U and J (upper left) and values of U and J for each line given in the upper right. DOS in the d_{xy} orbital depending on ϵ (lower left) and theoretically predicted enhancement of Λ_c due to uniaxial strain as a function of its value for $\epsilon_{xx} = 0$ (lower right). Each dotted line in the upper left plot corresponds to one $U - J$ combination given in the upper right. There is a clear correlation between $\Lambda_c(\epsilon_{xx} = 0)$ and the ratio of increase in T_c which can be seen in both the upper left and lower right panels. The experimental data points in the lower right plot are extracted from [33]. A proposed mechanism that explains this enhancement is detailed in the text.

strain is irrelevant since the vHs is not resolved, i.e. the DOS at the Fermi level does not change under strain. The lower Λ_c , the sharper the vHs will become. Therefore, its

shift enhances the DOS at the FS more strongly which in turn leads to a larger increase of T_c . Thus, a lower $\Lambda_c(\epsilon_{xx} = 0)$ yields an enhancement of T_c with ϵ_{xx} which is both larger and taking place over a narrower range of strain. Once the vHs has crossed the Fermi level, T_c is expected to go down again since we rapidly reduce the DOS at the Fermi level when straining further. Note that the nesting which generates the attractive interaction is not strongly asymmetric under strain, as can be seen in Fig. 1. Therefore, it cannot explain the asymmetry of Λ_c observed in Fig. 4. However, the density of states is asymmetric, see Fig. 4, giving rise to the observed asymmetry in Λ_c .

To compare our results to experiments, we evaluate $\Lambda_c(\epsilon_{xx}^{\text{vHs}})/\Lambda_c(\epsilon_{xx} = 0)$ and plot it versus $\Lambda_c(\epsilon_{xx} = 0)$, hence measuring the increase of the critical scale depending on the initial one. We extract the corresponding experimental values from Ref. 33 by calculating the ratio of the maximal T_c and the T_c at $\epsilon_{xx} = 0$. These results are summarized in Fig. 4. We observe that the experiments indeed fit to the data predicted by FRG and we can extract a line of U and J combinations along which the experiment is reproduced. We find that the values on the line are around $U = 1.1, 1.4$ eV and $J = 0.143 U, 0.1 U$. Again, we emphasize that these should be considered as effective values valid within our FRG formalism.

DISCUSSION

In summary, we studied SRO starting from a first-principles description of its electronic structure and using a diagrammatically unbiased FRG approach. Using

this framework, we investigated the influence of uniaxial strain as well as different contributions of Hund's coupling. We identified that the inter-orbital interaction reduction due to the density-density term J_{dd} is the main driving force favoring superconducting order, which we found to be a pseudospin-singlet $d_{x^2-y^2}$. Lastly, we showed that the experimental increase of T_c as a function of strain can be recovered on a quantitative level from FRG simulations and from a comparison to these experiments we extracted effective values of the interaction parameters.

Our results highlight the dominance of a single $d_{x^2-y^2}$ SCOP that transforms like the B_{1g} representation (A_g under uniaxial strain). We note that, while this SCOP agrees with many experimental measurements, it cannot explain the evidence for two-components and time-reversal symmetry breaking. From the experimentally observed behavior of the time-reversal symmetry condition, we can infer that a partner of our found SCOP is required to remain invariant under moving the vHs through the Fermi level. This condition would be for example fulfilled by states with nodal lines along the x direction [60, 61] or odd-frequency superconductors [68, 69].

An interesting direction for future studies would be to investigate the effect of interaction terms consistent with D_{4h} symmetry but breaking full cubic symmetry. This could potentially influence the competition between different low energy orders [80]. There are also many potential routes towards a more accurate investigation of the superconducting state. First, even though SRO is nearly perfectly layered, including the third spatial dimension increases the number of allowed ordering types [73]. Secondly, taking into account the frequency-dependence of the gap function and self-energy would allow to gauge the relevance of the proposed odd-frequency state. Finally, an important advance would be to start the FRG flow from a correlated starting point *i.e.* from dressed quasiparticles and their effective interactions. This could for example be achieved by starting the FRG from a DMFT [116] description of the normal state.

METHODS

Density functional Theory. — We use density functional theory [117–119] and the Quantum ESPRESSO DFT package [120, 121] with the PBE exchange-correlation functional [122] to calculate the electronic structure. Cell parameters and internal coordinates of the crystal structure in the $I4/mmm$ space group are relaxed in the conventional cell until all force components are smaller than 1 mRy/ a_0 (a_0 : Bohr radius) and all components of the stress tensor are smaller than 0.5 kbar, yielding a relaxed in-plane (out-of-plane) lattice constant of $a_0 = 3.878 \text{ \AA}$ ($c = 12.900 \text{ \AA}$). To calculate the strained structures, we fix one in-plane lattice constant of the conventional cell to the strained value, $a_{\text{new}} = (1 - s)a_0$, and relax the two orthogonal cell parameters as well as

the internal coordinates as described above. After relaxation, we use the corresponding primitive unit cells containing one ruthenium atom each, *i.e.* three t_{2g} orbitals. We use scalar-relativistic ultrasoft pseudopotentials from the GBRV library [123], with the $4s$ and $4p$ ($2s$) semicore states for both strontium and ruthenium (for oxygen) atoms included in the valence. In the scalar-relativistic approximation, the spin-orbit coupling term is dropped [124]. The energy cutoffs for the wave functions and charge density are set to 60 Ry and 720 Ry, respectively. We use a $12 \times 12 \times 12$ Monkhorst–Pack k -point grid to sample the Brillouin zone, and a smearing of 0.01 Ry utilizing the Methfessel–Paxton scheme. To describe the low-energy physics we construct three ruthenium-centered t_{2g} -like maximally localized Wannier functions for each strained structure using Wannier90 [125–127]. Spin-orbit coupling is included by first performing the DFT calculation without it and then adding a local SOC $\lambda_{\text{SOC}} = 200 \text{ meV}$ to account for the correlation-induced enhancement over the DFT value.

Functional renormalization group. — In order to account for strong local electronic correlations in this multi-orbital system, we consider the Hubbard-Kanamori interaction Hamiltonian [88]

$$\begin{aligned} \hat{H}_{\text{int}} = & \sum_{i1} U \hat{n}_{i1}^{\uparrow} \hat{n}_{i1}^{\downarrow} + \sum_{i1 \neq i2} (U - 2J_{\text{dd}}) \hat{n}_{i1}^{\uparrow} \hat{n}_{i2}^{\downarrow} \\ & + \sum_{i\sigma_1 \neq i\sigma_2} (U - 3J_{\text{dd}}) \hat{n}_{i1}^{\sigma_1} \hat{n}_{i2}^{\sigma_2} \\ & - \sum_{i1 \neq i2} J_{\text{ss}} \hat{c}_{i1}^{\uparrow, \dagger} \hat{c}_{i1}^{\downarrow} \hat{c}_{i2}^{\downarrow, \dagger} \hat{c}_{i2}^{\uparrow} + \sum_{i1 \neq i2} J_{\text{ss}} \hat{c}_{i1}^{\uparrow, \dagger} \hat{c}_{i1}^{\downarrow} \hat{c}_{i2}^{\downarrow} \hat{c}_{i2}^{\uparrow} \end{aligned} \quad (1)$$

where U is the intra-orbital on-site Coulomb repulsion, while J_{dd} (J_{ss}) is the density-density (spin-flip and pair hopping) part of the Hund's coupling. In the rotationally invariant formulation where $O(3)$ symmetry is satisfied, $J_{\text{dd}} = J_{\text{ss}} = J$. Although usually equal, the distinct effect of J_{dd} and J_{ss} when they are treated independently is discussed in Appendix B. Our calculations are performed in the regime of $U/W = 0.3 - 0.5$, with W being the total bandwidth and U being the Hubbard interaction. We restrict ourselves to a situation with an on-site Hubbard-Kanamori interaction, as with this type of interaction, we reproduce the dominant spin-spin susceptibilities peak position in comparison to the interacting spin-spin susceptibility measured in neutron scattering experiments [102], see App. B. Any interaction resulting in an analog peak structure should give the same physical results, as we argue in App. E.

The strong electronic correlations emerging from the Hubbard-Kanamori interactions are incorporated to the non-interacting downfolded systems using the functional renormalization group (FRG) [74, 128]. FRG is technically an exact method to calculate the effective action functional of a given quantum action. It does so by introducing a scale-dependent cutoff (here we use a sharp energy cutoff) in the non-interacting propagator of the system. By taking derivatives with respect to this cut-

off, one generates an infinite hierarchy of flow equations. In practice, this hierarchy must be truncated to become numerically tractable, making the method perturbatively motivated.

In this work, we employ the standard level-2 truncation, neglecting all three and more particle vertices. The validity of this approximation in the weak-to-intermediate coupling regime can be motivated by a power-counting argument to prove the RG-irrelevance of higher order terms [74]. Furthermore, we neglect the frequency dependence of the interaction, again motivated by the power counting argument, and the self-energy. This approach was applied to various systems including SRO [46, 48, 76–78, 89–100] and can be viewed as an diagrammatically unbiased extension of the random phase approximation.

In practice, we solve the flow equations from an energy scale much larger than the bandwidth and then integrate towards lower energies until we hit a divergence in one of the three diagrammatic channels labelled the particle-particle (PP), particle-hole (PH) and crossed particle-hole ($\overline{\text{PH}}$) channels. A divergence is associated to a phase transition as the corresponding susceptibility also diverges. Information of the ordering type can be extracted from the susceptibilities as well as linearized gap equations [129].

We employ the truncated unity approximation which allows us to reduce the memory required computationally [130–132].

For the FRG simulations, we use the TU²FRG code [132]. For convergence, we include all form-factors up to a distance of 8.2 Å, which amounts to a total number of 75 basis functions per orbital in the unit cell, i.e. all lattice harmonics up to the fifth (sixth) are included (depending on whether the constant is counted as harmonic or not). We checked for convergence by increasing the number of form-factors included near the phase transition

between the magnetic and the superconducting phase for a few data points in the phase diagram. The simulations are performed on a 36×36 momentum-mesh in the $x - y$ plane for the vertex function. The loop integration is performed using a FFT approach and an additional refinement of 45×45 is employed to achieve higher energy resolution. The results of the integration do not differ upon changing the resolution of the loop integration.

By using an enhanced value of the SOC, the effects of local interactions on SOC are already included on the single-particle level of the calculations. We do not suffer from double counting at that level since we neglect the flow of the self-energy. As a consequence however, our calculation does not take into account the renormalized effective mass of quasi-particles.

Acknowledgments. — JBP thanks Prof. E. Pavarini, Friedrich Krien, Lennart Klebl and Jacob Beyer for helpful discussion. The authors gratefully acknowledge the computing time granted through JARA on the supercomputer JURECA [133] at Forschungszentrum Jülich. JBP and DMK are supported by the Deutsche Forschungsgemeinschaft (DFG, German Research Foundation) under RTG 1995, within the Priority Program SPP 2244 “2DMP” — 443273985 and under Germany’s Excellence Strategy - Cluster of Excellence Matter and Light for Quantum Computing (ML4Q) EXC 2004/1 - 390534769. The Flatiron Institute is a division of the Simons Foundation.

Competing Interest. — The Authors declare no Competing Financial or Non-Financial Interests.

Data availability. — All simulation data is available upon reasonable request.

Code availability. — The codes used for simulation are open source packages and as such freely available.

Author Contributions. — SB performed the DFT simulations. JBP performed the FRG simulations. JBP, AG and OG analyzed the results. All authors contributed in writing the Manuscript.

-
- [1] Maeno, Y. *et al.* Superconductivity in a layered perovskite without copper. *Nature* **372**, 532–534 (1994).
- [2] Rice, T. & Sigrist, M. Sr₂RuO₄: an electronic analogue of ³He? *J. Condens. Matter Phys.* **7**, L643 (1995).
- [3] Ishida, K. *et al.* Spin-triplet superconductivity in Sr₂RuO₄ identified by ¹⁷O knight shift. *Nature* **396**, 658–660 (1998).
- [4] Ishida, K. *et al.* Spin polarization enhanced by spin-triplet pairing in Sr₂RuO₄ probed by NMR. *Phys. Rev. B* **92**, 100502 (2015).
- [5] Duffy, J. A. *et al.* Polarized-neutron scattering study of the cooper-pair moment in Sr₂RuO₄. *Phys. Rev. Lett.* **85**, 5412–5415 (2000).
- [6] Braden, M. *et al.* Inelastic neutron scattering study of magnetic excitations in Sr₂RuO₄. *Phys. Rev. B* **66**, 064522 (2002).
- [7] Liu, Y., Nelson, K., Mao, Z., Jin, R. & Maeno, Y. Tunneling and phase-sensitive studies of the pairing symmetry in Sr₂RuO₄. *J. Low Temp. Phys.* **131**, 1059–1068 (2003).
- [8] Nelson, K., Mao, Z., Maeno, Y. & Liu, Y. Odd-parity superconductivity in Sr₂RuO₄. *Science* **306**, 1151–1154 (2004).
- [9] Liu, Y. Phase-sensitive-measurement determination of odd-parity, spin-triplet superconductivity in Sr₂RuO₄. *NJP* **12**, 075001 (2010).
- [10] Deguchi, K., Mao, Z. Q., Yaguchi, H. & Maeno, Y. Gap structure of the spin-triplet superconductor Sr₂RuO₄ determined from the field-orientation dependence of the specific heat. *Phys. Rev. Lett.* **92**, 047002 (2004).
- [11] Lupien, C. *et al.* Ultrasound attenuation in Sr₂RuO₄: An angle-resolved study of the superconducting gap function. *Phys. Rev. Lett.* **86**, 5986–5989 (2001).
- [12] Xia, J., Maeno, Y., Beyersdorf, P. T., Fejer, M. M. & Kapitulnik, A. High resolution polar kerr effect measurements of Sr₂RuO₄: Evidence for broken time-

- reversal symmetry in the superconducting state. *Phys. Rev. Lett.* **97**, 167002 (2006).
- [13] Luke, G. M. *et al.* Time-reversal symmetry-breaking superconductivity in Sr_2RuO_4 . *Nature* **394**, 558–561 (1998).
- [14] Mackenzie, A. P. & Maeno, Y. The superconductivity of Sr_2RuO_4 and the physics of spin-triplet pairing. *Rev. Mod. Phys.* **75**, 657–712 (2003).
- [15] Maeno, Y., Kittaka, S., Nomura, T., Yonezawa, S. & Ishida, K. Evaluation of spin-triplet superconductivity in Sr_2RuO_4 . *JPSJ* **81**, 011009 (2012).
- [16] Izawa, K. *et al.* Superconducting gap structure of spin-triplet superconductor Sr_2RuO_4 studied by thermal conductivity. *Phys. Rev. Lett.* **86**, 2653–2656 (2001).
- [17] Hassinger, E. *et al.* Vertical line nodes in the superconducting gap structure of Sr_2RuO_4 . *Phys. Rev. X* **7**, 011032 (2017).
- [18] Tanatar, M. A. *et al.* Anisotropy of magnetothermal conductivity in Sr_2RuO_4 . *Phys. Rev. Lett.* **86**, 2649–2652 (2001).
- [19] Nishizaki, S., Maeno, Y. & Mao, Z. Changes in the superconducting state of Sr_2RuO_4 under magnetic fields probed by specific heat. *JPSJ* **69**, 572–578 (2000).
- [20] Jerzembeck, F. *et al.* Upper critical field of Sr_2RuO_4 under in-plane uniaxial pressure. *Phys. Rev. B* **107**, 064509 (2023).
- [21] Kittaka, S. *et al.* Sharp magnetization jump at the first-order superconducting transition in Sr_2RuO_4 . *Phys. Rev. B* **90**, 220502 (2014).
- [22] Yonezawa, S., Kajikawa, T. & Maeno, Y. Specific-heat evidence of the first-order superconducting transition in Sr_2RuO_4 . *JPSJ* **83**, 083706 (2014).
- [23] Kinjo, K. *et al.* Superconducting spin smecticity evidencing the Fulde-Ferrell-Larkin-Ovchinnikov state in Sr_2RuO_4 . *Science* **376**, 397–400 (2022).
- [24] Kirtley, J. R. *et al.* Upper limit on spontaneous supercurrents in Sr_2RuO_4 . *Phys. Rev. B* **76**, 014526 (2007).
- [25] Hicks, C. W. *et al.* Limits on superconductivity related magnetization in Sr_2RuO_4 and $\text{PrOs}_4\text{Sb}_{12}$ from scanning squid microscopy. *Phys. Rev. B* **81**, 214501 (2010).
- [26] Curran, P. J. *et al.* Search for spontaneous edge currents and vortex imaging in Sr_2RuO_4 mesostructures. *Phys. Rev. B* **89**, 144504 (2014).
- [27] Kreisel, A. *et al.* Quasi-particle interference of the van Hove singularity in Sr_2RuO_4 . *npj Quantum Mater.* **6** (2021).
- [28] Scaffidi, T. & Simon, S. H. Large chern number and edge currents in Sr_2RuO_4 . *Phys. Rev. Lett.* **115**, 087003 (2015).
- [29] Pustogow, A. *et al.* Constraints on the superconducting order parameter in Sr_2RuO_4 from oxygen-17 nuclear magnetic resonance. *Nature* **574**, 72–75 (2019).
- [30] Ishida, K., Manago, M., Kinjo, K. & Maeno, Y. Reduction of the ^{17}O knight shift in the superconducting state and the heat-up effect by NMR pulses on Sr_2RuO_4 . *JPSJ* **89**, 034712 (2020).
- [31] Petsch, A. N. *et al.* Reduction of the spin susceptibility in the superconducting state of Sr_2RuO_4 observed by polarized neutron scattering. *Phys. Rev. Lett.* **125**, 217004 (2020).
- [32] Watson, C. A., Gibbs, A. S., Mackenzie, A. P., Hicks, C. W. & Moler, K. A. Micron-scale measurements of low anisotropic strain response of local T_c in Sr_2RuO_4 . *Phys. Rev. B* **98**, 094521 (2018).
- [33] Steppke, A. *et al.* Strong peak in T_c of Sr_2RuO_4 under uniaxial pressure. *Science* **355**, eaaf9398 (2017).
- [34] Chronister, A. *et al.* Tuning the fermi liquid crossover in Sr_2RuO_4 with uniaxial stress. *npj Quantum Mater.* **7** (2022).
- [35] Sunko, V. *et al.* Direct observation of a uniaxial stress-driven Lifshitz transition in Sr_2RuO_4 . *npj Quantum Mater.* **4**, 46 (2019).
- [36] Benhabib, S. *et al.* Ultrasound evidence for a two-component superconducting order parameter in Sr_2RuO_4 . *Nat. Phys.* **17**, 194–198 (2021).
- [37] Ghosh, S. *et al.* Thermodynamic evidence for a two-component superconducting order parameter in Sr_2RuO_4 . *Nat. Phys.* **17**, 199–204 (2021).
- [38] Grinenko, V. *et al.* Split superconducting and time-reversal symmetry-breaking transitions in Sr_2RuO_4 under stress. *Nat. Phys.* **17**, 748–754 (2021).
- [39] Grinenko, V. *et al.* μSR measurements on Sr_2RuO_4 under $\langle 110 \rangle$ uniaxial stress. *Phys. Rev. B* **107**, 024508 (2023).
- [40] Li, Y.-S. *et al.* High-sensitivity heat-capacity measurements on Sr_2RuO_4 under uniaxial pressure. *PNAS* **118**, e2020492118 (2021).
- [41] Li, Y.-S. *et al.* Elastocaloric determination of the phase diagram of Sr_2RuO_4 . *Nature* **607**, 276–280 (2022).
- [42] Palle, G. *et al.* Constraints on the superconducting state of Sr_2RuO_4 from elastocaloric measurements. *Phys. Rev. B* **108**, 094516 (2023).
- [43] Mueller, E. *et al.* Constraints on a split superconducting transition under uniaxial strain in Sr_2RuO_4 from scanning squid microscopy. *Phys. Rev. B* **108**, 144501 (2023).
- [44] Mackenzie, A. P., Scaffidi, T., Hicks, C. W. & Maeno, Y. Even odder after twenty-three years: the superconducting order parameter puzzle of Sr_2RuO_4 . *npj Quantum Mater.* **2**, 40 (2017).
- [45] Raghu, S., Kapitulnik, A. & Kivelson, S. A. Hidden quasi-one-dimensional superconductivity in Sr_2RuO_4 . *Phys. Rev. Lett.* **105**, 136401 (2010).
- [46] Wang, Q. *et al.* Theory of superconductivity in a three-orbital model of Sr_2RuO_4 . *EPL* **104**, 17013 (2013).
- [47] Tsuchiizu, M., Yamakawa, Y., Onari, S., Ohno, Y. & Kontani, H. Spin-triplet superconductivity in Sr_2RuO_4 due to orbital and spin fluctuations: Analyses by two-dimensional renormalization group theory and self-consistent vertex-correction method. *Phys. Rev. B* **91**, 155103 (2015).
- [48] Wang, W.-S., Zhang, C.-C., Zhang, F.-C. & Wang, Q.-H. Theory of chiral p -wave superconductivity with near nodes for Sr_2RuO_4 . *Phys. Rev. Lett.* **122**, 027002 (2019).
- [49] Zhang, L.-D., Huang, W., Yang, F. & Yao, H. Superconducting pairing in Sr_2RuO_4 from weak to intermediate coupling. *Phys. Rev. B* **97**, 060510 (2018).
- [50] Scaffidi, T., Romers, J. C. & Simon, S. H. Pairing symmetry and dominant band in Sr_2RuO_4 . *Phys. Rev. B* **89**, 220510 (2014).
- [51] Ramires, A. & Sigrist, M. Identifying detrimental effects for multiorbital superconductivity: Application to Sr_2RuO_4 . *Phys. Rev. B* **94**, 104501 (2016).
- [52] Acharya, S. *et al.* Evening out the spin and charge parity to increase t_c in Sr_2RuO_4 . *Commun. phys.* **2**, 163 (2019).

- [53] Rømer, A. T., Hirschfeld, P. J. & Andersen, B. M. Superconducting state of Sr_2RuO_4 in the presence of longer-range Coulomb interactions. *Phys. Rev. B* **104** (2021).
- [54] Rømer, A. T., Maier, T. A., Kreisel, A., Hirschfeld, P. J. & Andersen, B. M. Leading superconducting instabilities in three-dimensional models for Sr_2RuO_4 . *Phys. Rev. Research* **4**, 033011 (2022).
- [55] Moon, C.-Y. Effects of orbital selective dynamical correlation on the spin susceptibility and superconducting symmetries in sr_2ruo_4 . *Phys. Rev. Research* **5**, L022058 (2023).
- [56] Røising, H. S., Wagner, G., Roig, M., Rømer, A. T. & Andersen, B. M. Heat capacity double transitions in time-reversal symmetry broken superconductors. *Phys. Rev. B* **106**, 174518 (2022).
- [57] Kivelson, S. A., Yuan, A. C., Ramshaw, B. & Thomale, R. A proposal for reconciling diverse experiments on the superconducting state in Sr_2RuO_4 . *npj Quantum Mater.* **5** (2020).
- [58] Sheng, Y., Li, Y. & Yang, Y.-f. Multipole-fluctuation pairing mechanism of $d_{x^2-y^2} + ig$ superconductivity in Sr_2RuO_4 . *Phys. Rev. B* **106**, 054516 (2022).
- [59] Wang, X., Wang, Z. & Kallin, C. Higher angular momentum pairing states in Sr_2RuO_4 in the presence of longer-range interactions. *Phys. Rev. B* **106**, 134512 (2022).
- [60] Yuan, A. C., Berg, E. & Kivelson, S. A. Strain-induced time reversal breaking and half quantum vortices near a putative superconducting tetracritical point in sr_2ruo_4 . *Phys. Rev. B* **104**, 054518 (2021).
- [61] Yuan, A. C., Berg, E. & Kivelson, S. A. Multiband mean-field theory of the $d + ig$ superconductivity scenario in sr_2ruo_4 . *Phys. Rev. B* **108**, 014502 (2023).
- [62] Scaffidi, T. Degeneracy between even- and odd-parity superconductivity in the quasi-one-dimensional Hubbard model and implications for Sr_2RuO_4 . *Phys. Rev. B* **107**, 014505 (2023).
- [63] Kaba, S.-O. & Sénéchal, D. Group-theoretical classification of superconducting states of strontium ruthenate. *Phys. Rev. B* **100** (2019).
- [64] Ando, S., Ikegaya, S., Tamura, S., Tanaka, Y. & Yada, K. Surface state of the interorbital pairing state in the sr_2ruo_4 superconductor. *Phys. Rev. B* **106**, 214520 (2022).
- [65] Nica, E. M. & Si, Q. Multiorbital singlet pairing and $d+d$ superconductivity. *npj Quantum Mater.* **6** (2021).
- [66] Deisz, J. J. & Kidd, T. E. Quantum many-body calculation of mixed-parity pairing in the sr_2ruo_4 superconductor induced by spin-orbit coupling. *Phys. Rev. Lett.* **107**, 277003 (2011).
- [67] Gingras, O., Nourafkan, R., Tremblay, A.-M. S. & Côté, M. Superconducting Symmetries of Sr_2RuO_4 from First-Principles Electronic Structure. *Phys. Rev. Lett.* **123**, 217005 (2019).
- [68] Gingras, O., Allaglo, N., Nourafkan, R., Côté, M. & Tremblay, A.-M. S. Superconductivity in correlated multiorbital systems with spin-orbit coupling: Coexistence of even- and odd-frequency pairing, and the case of Sr_2RuO_4 . *Phys. Rev. B* **106**, 064513 (2022).
- [69] Gingras, O., Georges, A. & Parcollet, O. Frequency-Dependent Superconducting States From the Two-Time Linear Response Theory: Application To Sr_2RuO_4 (2023). 2312.15074.
- [70] Suh, H. G. *et al.* Stabilizing even-parity chiral superconductivity in Sr_2RuO_4 . *Phys. Rev. Research* **2**, 032023 (2020).
- [71] Beck, S., Hampel, A., Zingl, M., Timm, C. & Ramires, A. Effects of strain in multiorbital superconductors: The case of Sr_2RuO_4 . *Phys. Rev. Research* **4**, 023060 (2022).
- [72] Huang, W. & Yao, H. Possible Three-Dimensional Nematic Odd-Parity Superconductivity in Sr_2RuO_4 . *Phys. Rev. Lett.* **121**, 157002 (2018).
- [73] Ramires, A. & Sigrist, M. Superconducting order parameter of Sr_2RuO_4 : A microscopic perspective. *Phys. Rev. B* **100**, 104501 (2019).
- [74] Metzner, W., Salmhofer, M., Honerkamp, C., Meden, V. & Schönhammer, K. Functional renormalization group approach to correlated fermion systems. *RMP* **84**, 299–352 (2012).
- [75] Kohn, W. & Sham, L. J. Self-consistent equations including exchange and correlation effects. *Phys. Rev.* **140**, A1133–A1138 (1965).
- [76] Liu, Y.-C., Zhang, F.-C., Rice, T. M. & Wang, Q.-H. Theory of the evolution of superconductivity in Sr_2RuO_4 under anisotropic strain. *npj Quantum Mater.* **2** (2017).
- [77] Wang, Z., Wang, X. & Kallin, C. Spin-orbit coupling and spin-triplet pairing symmetry in Sr_2RuO_4 . *Phys. Rev. B* **101**, 064507 (2020).
- [78] Liu, Y.-C., Wang, W.-S., Zhang, F.-C. & Wang, Q.-H. Superconductivity in Sr_2RuO_4 thin films under biaxial strain. *Phys. Rev. B* **97**, 224522 (2018).
- [79] Tamai, A. *et al.* High-Resolution Photoemission on Sr_2RuO_4 Reveals Correlation-Enhanced Effective Spin-Orbit Coupling and Dominantly Local Self-Energies. *Phys. Rev. X* **9**, 021048 (2019).
- [80] Zhang, G., Gorelov, E., Sarvestani, E. & Pavarini, E. Fermi surface of Sr_2RuO_4 : Spin-orbit and anisotropic coulomb interaction effects. *Phys. Rev. Lett.* **116**, 106402 (2016).
- [81] Kim, M., Mravlje, J., Ferrero, M., Parcollet, O. & Georges, A. Spin-orbit coupling and electronic correlations in sr_2ruo_4 . *Phys. Rev. Lett.* **120**, 126401 (2018).
- [82] Veenstra, C. N. *et al.* Spin-orbital entanglement and the breakdown of singlets and triplets in sr_2ruo_4 revealed by spin- and angle-resolved photoemission spectroscopy. *Phys. Rev. Lett.* **112**, 127002 (2014).
- [83] Haverkort, M. W., Elfimov, I. S., Tjeng, L. H., Sawatzky, G. A. & Damascelli, A. Strong spin-orbit coupling effects on the fermi surface of sr_2ruo_4 and sr_2rho_4 . *Phys. Rev. Lett.* **101**, 026406 (2008).
- [84] Pavarini, E. & Mazin, I. I. First-principles study of spin-orbit effects and NMR in Sr_2RuO_4 . *Phys. Rev. B* **74**, 035115 (2006).
- [85] Damascelli, A. *et al.* Fermi surface, surface states, and surface reconstruction in Sr_2RuO_4 . *Phys. Rev. Lett.* **85**, 5194–5197 (2000).
- [86] Barber, M. E. *et al.* Role of correlations in determining the van hove strain in sr_2ruo_4 . *Phys. Rev. B* **100**, 245139 (2019).
- [87] Unpublished DMFT data shows that the corrections of the SOC due to strain are negligible.
- [88] Kanamori, J. Electron correlation and ferromagnetism of transition metals. *Prog. Theor. Phys.* **30**, 275–289 (1963).

- [89] Scherer, M. M., Kennes, D. M. & Classen, L. Chiral superconductivity with enhanced quantized hall responses in moiré transition metal dichalcogenides. *npj Quantum Mater.* **7**, 100 (2022).
- [90] Klebl, L., Fischer, A., Classen, L., Scherer, M. M. & Kennes, D. M. Competition of density waves and superconductivity in twisted tungsten diselenide. *Phys. Rev. Research* **5** (2023).
- [91] Gneist, N., Classen, L. & Scherer, M. M. Competing instabilities of the extended hubbard model on the triangular lattice: Truncated-unity functional renormalization group and application to moiré materials. *Phys. Rev. B* **106**, 125141 (2022).
- [92] Kiesel, M. L., Platt, C., Hanke, W. & Thomale, R. Model evidence of an anisotropic chiral $d+id$ -wave pairing state for the water-intercalated $\text{Na}_x\text{CoO}_2\cdot y\text{H}_2\text{O}$ superconductor. *Phys. Rev. Lett.* **111**, 097001 (2013).
- [93] Kiesel, M. L., Platt, C. & Thomale, R. Unconventional fermi surface instabilities in the kagome hubbard model. *Phys. Rev. Lett.* **110**, 126405 (2013).
- [94] Beyer, J. *et al.* Rashba spin-orbit coupling in the square-lattice hubbard model: A truncated-unity functional renormalization group study. *Phys. Rev. B* **107**, 125115 (2023).
- [95] Kiesel, M. L., Platt, C., Hanke, W., Abanin, D. A. & Thomale, R. Competing many-body instabilities and unconventional superconductivity in graphene. *Phys. Rev. B* **86**, 020507 (2012).
- [96] Profe, J. B., Honerkamp, C., Achilles, S. & Kennes, D. M. Electronic instabilities in penrose quasicrystals: Competition, coexistence, and collaboration of order. *Phys. Rev. Research* **3** (2021).
- [97] Ehrlich, J. & Honerkamp, C. Functional renormalization group for fermion lattice models in three dimensions: Application to the hubbard model on the cubic lattice. *Phys. Rev. B* **102**, 195108 (2020).
- [98] Klebl, L., Kennes, D. M. & Honerkamp, C. Functional renormalization group for a large moiré unit cell. *Phys. Rev. B* **102**, 085109 (2020).
- [99] de la Peña, D. S., Lichtenstein, J., Honerkamp, C. & Scherer, M. M. Antiferromagnetism and competing charge instabilities of electrons in strained graphene from coulomb interactions. *Phys. Rev. B* **96**, 205155 (2017).
- [100] O, S.-J., Kim, Y.-H., Rim, H.-Y., Pak, H.-C. & Im, S.-J. Effect of exchange interaction on electronic instabilities in the honeycomb lattice: A functional renormalization group study. *Phys. Rev. B* **99**, 245140 (2019).
- [101] Iida, K. *et al.* Inelastic neutron scattering study of the magnetic fluctuations in Sr_2RuO_4 . *Phys. Rev. B* **84**, 060402 (2011).
- [102] Steffens, P. *et al.* Spin fluctuations in Sr_2RuO_4 from polarized neutron scattering: Implications for superconductivity. *Phys. Rev. Lett.* **122**, 047004 (2019).
- [103] Berezinskii, V. Destruction of long-range order in one-dimensional and two-dimensional systems having a continuous symmetry group i. classical systems. *Sov. Phys. JETP* **32**, 493–500 (1971).
- [104] Berezinskii, V. Destruction of long-range order in one-dimensional and two-dimensional systems possessing a continuous symmetry group. ii. quantum systems. *Sov. Phys. JETP* **34**, 610–616 (1972).
- [105] Kosterlitz, J. M. & Thouless, D. J. Ordering, metastability and phase transitions in two-dimensional systems. *J. Phys. C: Solid State Phys.* **6**, 1181 (1973).
- [106] Because of Mermin-Wagner theorem (which is not obeyed by FRG), a finite T_c is expected for the BKT transition into the SC phase, while $T_c = 0$ for an SDW breaking $SU(2)$.
- [107] Iida, K. *et al.* Two-dimensional incommensurate magnetic fluctuations in $\text{Sr}_2(\text{Ru}_{0.99}\text{Ti}_{0.01})\text{O}_4$. *JPSJ* **81**, 124710 (2012).
- [108] Strand, H. U. R., Zingl, M., Wentzell, N., Parcollet, O. & Georges, A. Magnetic response of Sr_2RuO_4 : Quasi-local spin fluctuations due to hund’s coupling. *Phys. Rev. B* **100** (2019).
- [109] Rømer, A. T. *et al.* Theory of strain-induced magnetic order and splitting of T_c and T_{trsb} in Sr_2RuO_4 . *Phys. Rev. B* **102**, 054506 (2020).
- [110] Kim, B., Khmelevskiy, S., Franchini, C. & Mazin, I. I. Suppressed fluctuations as the origin of the static magnetic order in strained sr_2ruo_4 . *Phys. Rev. Lett.* **130**, 026702 (2023).
- [111] Hille, C. *et al.* Quantitative functional renormalization group description of the two-dimensional hubbard model. *Phys. Rev. Research* **2** (2020).
- [112] Roig, M., Rømer, A. T., Kreisel, A., Hirschfeld, P. J. & Andersen, B. M. Superconductivity in multiorbital systems with repulsive interactions: Hund’s pairing versus spin-fluctuation pairing. *Phys. Rev. B* **106**, L100501 (2022).
- [113] Wang, J., Eberlein, A. & Metzner, W. Competing order in correlated electron systems made simple: Consistent fusion of functional renormalization and mean-field theory. *Phys. Rev. B* **89**, 121116 (2014).
- [114] Again we stress that Λ_c is not to be confused with the leading eigenvalue from an Eliashberg calculation λ . Most importantly, we have $\Lambda_c \propto T_c$ instead of the exponential suppression from the gap equation.
- [115] Lindquist, A. W. & Kee, H.-Y. Distinct reduction of knight shift in superconducting state of sr_2ruo_4 under uniaxial strain. *Phys. Rev. Research* **2**, 032055 (2020).
- [116] Taranto, C. *et al.* From infinite to two dimensions through the functional renormalization group. *Phys. Rev. Lett.* **112**, 196402 (2014).
- [117] Kohn, W. & Sham, L. J. Self-Consistent Equations Including Exchange and Correlation Effects. *Phys. Rev.* **140**, A1133–A1138 (1965).
- [118] Hohenberg, P. & Kohn, W. Inhomogeneous Electron Gas. *Phys. Rev.* **136**, B864–B871 (1964).
- [119] Kohn, W., Becke, A. D. & Parr, R. G. Density Functional Theory of Electronic Structure. *J. Phys. Chem.* **100**, 12974–12980 (1996).
- [120] Giannozzi, P. *et al.* Quantum espresso: a modular and open-source software project for quantum simulations of materials. *J. Condens. Matter Phys.* **21**, 395502 (2009).
- [121] Giannozzi, P. *et al.* Advanced capabilities for materials modelling with quantum ESPRESSO. *J. Condens. Matter Phys.* **29**, 465901 (2017).
- [122] Perdew, J. P., Burke, K. & Ernzerhof, M. Generalized gradient approximation made simple. *Phys. Rev. Lett.* **77**, 3865–3868 (1996).
- [123] Garrity, K. F., Bennett, J. W., Rabe, K. M. & Vanderbilt, D. Pseudopotentials for high-throughput dft calculations. *Comput. Mater. Sci.* **81**, 446 – 452 (2014).
- [124] Takeda, T. The scalar relativistic approximation. *Zeitschrift für Physik B Condensed Matter* **32**, 43–48 (1978).

- [125] Mostofi, A. A. *et al.* wannier90: A tool for obtaining maximally-localised wannier functions. *Comput. Phys. Commun.* **178**, 685–699 (2008).
- [126] Mostofi, A. A. *et al.* An updated version of wannier90: A tool for obtaining maximally-localised wannier functions. *Comput. Phys. Commun.* **185**, 2309–2310 (2014).
- [127] Pizzi, G. *et al.* Wannier90 as a community code: new features and applications. *J. Condens. Matter Phys.* **32**, 165902 (2020).
- [128] Dupuis, N. *et al.* The nonperturbative functional renormalization group and its applications. *Phys. Rep.* **910**, 1–114 (2021).
- [129] Beyer, J., Profe, J. B. & Klebl, L. Reference results for the momentum space functional renormalization group. *EPJ B* **95** (2022).
- [130] Husemann, C. & Salmhofer, M. Efficient parametrization of the vertex function, Ω scheme, and the t, t' Hubbard model at van hove filling. *Phys. Rev. B* **79**, 195125 (2009).
- [131] Lichtenstein, J. *et al.* High-performance functional Renormalization Group calculations for interacting fermions. *Comput. Phys. Commun.* **213**, 100 – 110 (2017).
- [132] Profe, J. B. & Kennes, D. M. TU²FRG: a scalable approach for truncated unity functional renormalization group in generic fermionic models. *EPJ B* **95** (2022).
- [133] Jülich Supercomputing Centre. JURECA: Data Centric and Booster Modules implementing the Modular Supercomputing Architecture at Jülich Supercomputing Centre. *JLSRF* **7** (2021).
- [134] Zabolotnyy, V. *et al.* Renormalized band structure of Sr₂RuO₄: A quasiparticle tight-binding approach. *J. Electron Spectros. Relat. Phenomena* **191**, 48–53 (2013).
- [135] Bickers, N. E. Self-Consistent Many-Body Theory for Condensed Matter Systems. In Sénéchal, D., Tremblay, A.-M. & Bourbonnais, C. (eds.) *Theoretical Methods for Strongly Correlated Electrons*, CRM Series in Mathematical Physics, 237–296 (Springer, 2004).

Appendix A: Low-energy tight-binding model

The tight-binding Hamiltonian used in this work, based on DFT and a correlation-enhanced SOC, reproduces the experimentally observed Fermi-surface of Ref. [79] as shown in Fig. 5. Furthermore, our DFT results are consistent with prior DFT results [55, 67] within the different spin orbit couplings considered. Larger differences arise in comparison with the Fermi surface in Refs. [115, 134], see Fig. 5. These works extracted a tight-binding model from fits to the Fermi surface measured in ARPES. However, recent advances in ARPES techniques allow a more precise measurement of the Fermi surface, explaining the difference to Ref. [134]. On the other hand Ref [115] fits to Tamai *et al.* [79], thereby obtaining a similar Fermi surface to the one presented here, however, with a much larger bandwidth. Since the fit is optimized for the Fermi surface only, the bandwidths of these models need not necessarily agree and are shown here for illustrative purposes only, in particular since some of the fits represent quasi-particle bands. A comparison of the

Fermi surface and bandstructure of this publication and various ARPES fits is shown in Fig. 5.

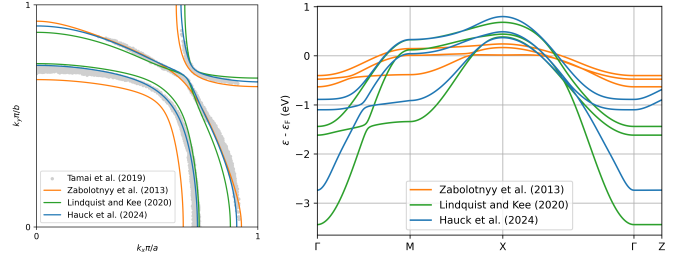


FIG. 5. **Comparison of non-interacting models.** Comparison of the Fermi-surface (left) and the bandstructure along the high-symmetry path (right) between this work, Zabolotnyy *et al.* [134], Lindquist and Kee [115] and the ARPES data from Ref. [79]. Note that we neglect the t_5 hopping in Ref. [115] as it was unclear to what term it corresponds.

Appendix B: Particle-hole susceptibility

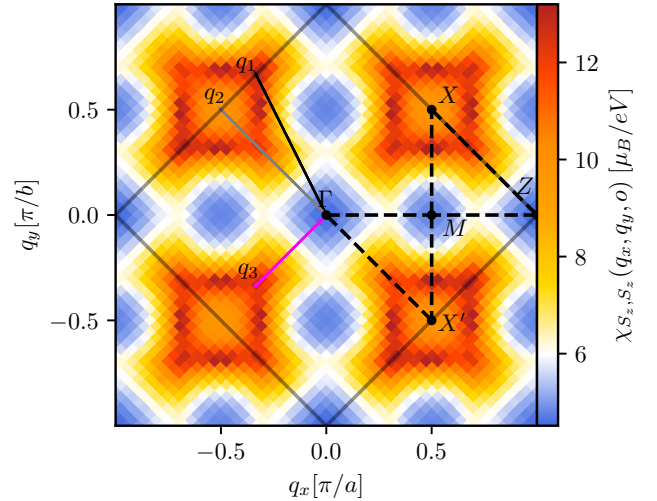


FIG. 6. **Interacting particle-hole susceptibility at $\Lambda = 464$ K obtained with FRG** at the extracted experimental interaction parameters $U = 1.1$ eV and $J = 0.143 U$. The color scale is adapted to the one of Ref. [108]. We again mark the first BZ as a black square and draw the $k_z = 0$ irreducible path as dotted lines.

In the main text, we explained how we can extract the value of effective parameters of the interaction suitable in FRG, here we found $U = 1.1$ eV and $J = 0.143 U$. With these extracted values, we compute the interacting particle-hole susceptibility χ_{PH} at $T = 464$ K, shown on a two-dimensional momentum-grid in Fig. 6. We compare with χ_{PH} obtained by solving the Bethe-Salpeter equation with a vertex extracted using DMFT [108]. FRG

clearly overestimates the correlations at the X -point and on the connection line between X and M , similarly to what is obtained using the random phase approximation [67, 68]. Beyond that, FRG reproduces roughly the same shape and structure of the susceptibility as DMFT, but cannot reproduce its shifting of the peaks [55, 108]. As discussed in App. E, correcting for this overestimation in the effective interaction might influence the critical energy scales, but is not expected to drastically alter the hierarchy of the different order parameters. Most critically, we show analytically that the leading SDW peak observed in experiments [102] will also lead to an attractive interaction in the singlet channel, see Appendix E.

Appendix C: Subleading instabilities

To estimate the minimal separation between the divergence of the leading and the subleading eigenvalue we track at which scale the subleading instability's magnitude is the same as the leading instabilities one, see Fig. 7. This estimate assumes that the subleading and leading divergences are behaving identically. As such it is an approximate lower bound for the separation. We find it to be consistently to be in the order of a few percent.

Prior FRG studies [46, 48, 78] predicted a leading p -wave divergence, which in our calculation is far subleading with at least 20 other even-parity eigenvectors between the leading and first odd-parity solution. Thus we can safely conclude that odd-parity is far from dominant. The difference in results to prior FRG studies can be traced back to a more refined non-interacting model. I.e. capturing the position of the largest peak observed in neutron diffraction is central to capture the leading contributions to the pairing in a spin fluctuation picture.

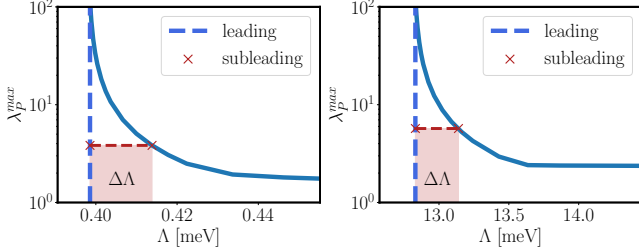


FIG. 7. **Estimating the separation between the critical scales for the leading and subleading instability** at $(U, J/U) = (1.3 \text{ eV}, 0.1625)$ (left) and $(U, J/U) = (1.5 \text{ eV}, 0.225)$ (right). The dashed vertical line marks the critical scale at the divergence. The value of the first subleading coupling is then extracted and tracked back to where the leading coupling had this value, this is shown in red. This gives us a lower bound on the separation of the divergent couplings. The separation is highlighted as the red area under the blue curve. This analysis gives a lower bound for the separation of the order of 2 to 3% under the assumption that the subleading coupling diverges at the same rate and with the same shape as the leading one.

Appendix D: Effects of J_{dd} and J_{ss}

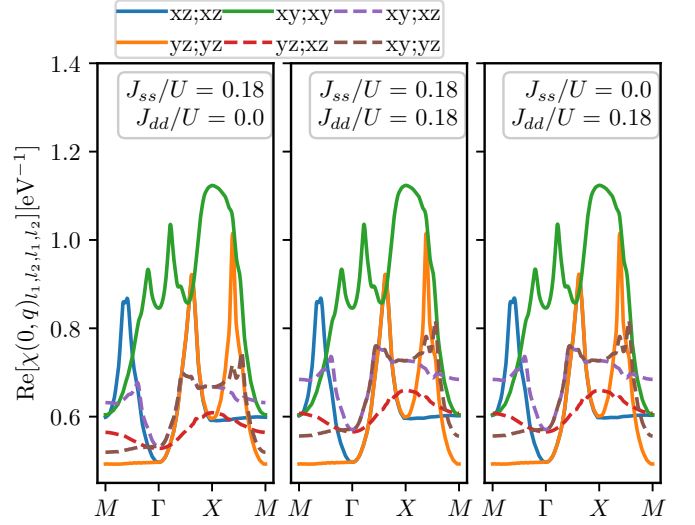


FIG. 8. **Effects of J_{dd} and J_{ss} on the interacting susceptibility** obtained from RPA at $U = 0.3 \text{ eV}$ and $\Lambda = 10 \text{ meV}$.

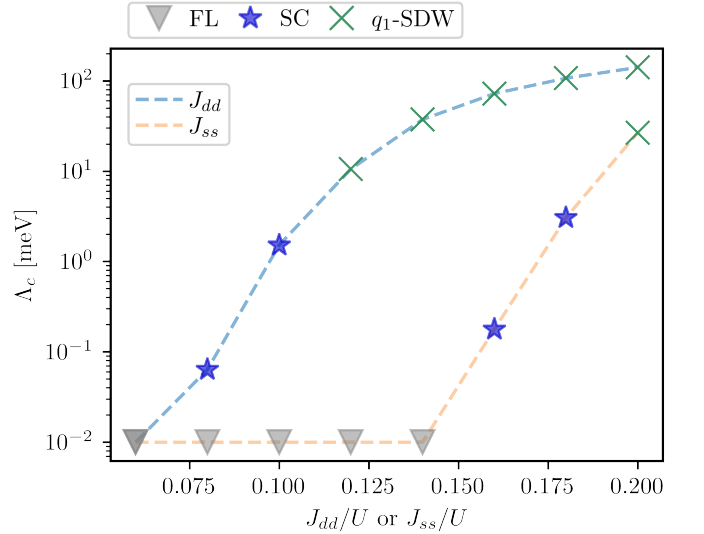


FIG. 9. **Effects of J_{dd} and J_{ss} on the FRG flow results.** We observe that J_{dd} drives the transition to an ordered state quicker than J_{ss} indicating that for the underlying interaction mechanism it is beneficial to have smaller inter-orbital coupling.

In the following, we analyze analytically the effects of J_{ss} and J_{dd} in a simplified $SU(2)$ symmetric two-orbital model. This model is oversimplified so the results are not directly applicable to SRO, however it does help to understand the way in which the different contributions can influence the low energy physics. The non-interacting model is assumed to be given by

$$\hat{H}_0 = \sum_l \sum_{ij} t_{ij} (c_{li}^\dagger c_{lj} + c_{lj}^\dagger c_{li}) \quad (\text{D1})$$

where l is an orbital and i, j are sites. We first examine the magnetic channel susceptibility which is given in the two-particle basis $|l_1\rangle \otimes |l_2\rangle$. The components of the bare particle-hole susceptibility are given by

$$[\chi_{\text{PH}}^0(Q)]_{KK'}^{l_1 l_2 l_3 l_4} \propto G_{K+Q}^{l_1 l_3} G_K^{l_4 l_2} \delta_{KK'} \quad (\text{D2})$$

where G is the one-particle Green's function and K, K' and Q are four-momenta [68, 135]. From this expression, we find that the bare particle-hole susceptibility is diagonal in orbital space. Presuming the two orbitals to be degenerate, we write

$$\chi_{\text{PH}}^0 = \begin{pmatrix} \chi_1 & 0 & 0 & 0 \\ 0 & \chi_2 & 0 & 0 \\ 0 & 0 & \chi_2 & 0 \\ 0 & 0 & 0 & \chi_1 \end{pmatrix}. \quad (\text{D3})$$

In RPA, the irreducible vertex in the particle-hole channel is the anti-symmetric static and local Coulomb tensor $\Gamma_{\text{PH}} = \Lambda_{\text{PH}}$. We spin-diagonalize it and take the magnetic channel such that $\Lambda_{\text{PH}}^m \equiv \Lambda_{\text{PH}}^{\uparrow\uparrow\uparrow\uparrow} - \Lambda_{\text{PH}}^{\uparrow\uparrow\downarrow\downarrow}$. It describes the irreducible set of particle-hole interactions that generates spin-fluctuations. As shown in the Appendix C of Ref. 68, it can be found, up to a minus sign due to conventions, as

$$\Lambda_{\text{PH}}^m = \begin{pmatrix} U & 0 & 0 & J_{ph} \\ 0 & U - 2J_{\text{dd}} & J_{sf} & 0 \\ 0 & J_{sf} & U - 2J_{\text{dd}} & 0 \\ J_{ph} & 0 & 0 & U \end{pmatrix}. \quad (\text{D4})$$

The parameters are the same as those characterizing the Hamiltonian of Eq. (1), in particular with the pair-hopping and spin-flip terms characterized by J_{ph} and J_{sf} respectively. Consequently, the eigenvalues of $\Lambda_{\text{PH}}^m \chi_{\text{PH}}^0$ which quantify the amount of spin-fluctuations are

$$\lambda = \chi_1(U \pm J_{ph}), \quad \chi_2(U - 2J_{\text{dd}} \pm J_{sf}) \quad (\text{D5})$$

with eigenvectors

$$\begin{pmatrix} 1 \\ 0 \\ 0 \\ \pm 1 \end{pmatrix} \quad \text{and} \quad \begin{pmatrix} 0 \\ 1 \\ \pm 1 \\ 0 \end{pmatrix}. \quad (\text{D6})$$

In other words, a pair on l_1 can constructively or destructively interfere with a pair on l_2 via J_{ph} , which enhances the intra-orbital components of the susceptibility.

On the other hand, J_{sf} enhances the inter-orbital components. On the other hand, J_{dd} acts in the same way as spin flips, affecting only the inter-orbital components of the interacting susceptibility. However it has twice the magnitude. Which terms play what role also crucially depends on the signs of χ_1 and χ_2 ;

The corresponding numerical experiments are visualized in Fig. 8. They quantify the effects of the two different couplings and help to gauge their importance for the phase diagram.

Appendix E: Driving fluctuations analysis

Here, we want to construct a more in depth understanding of which spin-fluctuations are responsible for which pairing instabilities. To this end, we focus on the d_{xy} orbital again assuming $SU(2)$ symmetry. Therefore we restrict the analysis to the spin-singlet sector. The spin-triplet can be obtained by employing the crossing relations. Furthermore, we assume an attractive interaction obtained from RPA like spin-fluctuation $C(q)$, i.e. without fermionic momentum dependencies. The starting point for this discussion is the linearized gap equation, which can be rewritten as

$$\lambda \Delta_{o_1, o_2}(k) = \Gamma_{o_1, o_2; o'_3, o'_4}^P(q=0, k, k') \times \chi_{o'_3, o'_4; o_3, o_4}(k') \Delta_{o_3, o_4}(k') \quad (\text{E1})$$

where summation over repeated indices is implicit. We arrive to a simpler picture by transforming this equation to real-space, introducing the lattice vectors b . We write

$$\Delta_{o_1, o_2}(b) = e^{-ik \cdot b} \Delta_{o_1, o_2}(k), \quad (\text{E2})$$

which leads us to

$$\lambda \Delta_{o_1, o_2}(b) = \Gamma_{o_1, o_2; o'_3, o'_4}^P(b, b') \times \chi_{o'_3, o'_4; o_3, o_4}(b', b'') \Delta_{o_3, o_4}(b''). \quad (\text{E3})$$

Now, we are mainly interested in nearest neighbor superconductivity, thus restricting the allowed b to nearest neighbor form-factors. The two central quantities in the linearized gap equation are the particle-particle loop $\chi_{o'_3, o'_4; o_3, o_4}(b', b'')$ and the P-channel vertex $\Gamma_{o_1, o_2; o'_3, o'_4}^P(b, b')$, which in the following we construct for a specific choice of a symmetrized basis for the $d_{x^2-y^2}$ and the extended s -wave SCOPs for a purely spin-fluctuation interaction $C(q_C = k + k' - q_P)$. For this we introduce the symmetrized form-factors denoted by $f_b(k)$:

$$\begin{aligned} \Gamma^P(q_P = 0, b, b) &= \frac{1}{4} \int dk dk' dr (\cos(k_x) \pm \cos(k_y)) (\cos(k'_x) \pm \cos(k'_y)) e^{ir(k+k')} C(r) \\ &= \frac{1}{4} [C(r_x = 1, r_y = 0) + C(r_x = -1, r_y = 0) + C(r_x = 0, r_y = 1) + C(r_x = 0, r_y = -1)]. \end{aligned} \quad (\text{E4})$$

From this we observe immediately two things: First, a

pure spin-spin interaction does not differentiate between

extended s -wave or $d_{x^2-y^2}$ (or p_x and p_y). It merely gives a numerical prefactor to be put into the gap equation. Secondly, that prefactor is just dependent on the value of $C(r)$ for r on the nearest neighbors; i.e. as long as the Fourier transform of C is attractive on the nearest neighbor, we generate superconductivity whose symmetry is determined by the particle-particle loops fermionic argument only.

$$C(r) = \int dq e^{iqr} C(q) \quad (\text{E5})$$

For now, let's assume that $C(q)$ (again we focus on the d_{xy} orbital) is consisting of δ -peaks at q_2 or q_1/q_3 with unit weight, for simplicity we furthermore go back to a square lattice unit cell. This allows us to calculate the Fourier transformation $C(r)$ analytically. We focus on $C(r_x = 1, r_y = 0)$, since all other terms can be understood via symmetries. We find $C(r_x = 1, r_y = 0; q_2) = -1$ and $C(r_x = 1, r_y = 0; q_1) = e^{i2\pi/3}$, meaning that $\Gamma^P(q_2) = -1$ and $\Gamma^P(q_1) = -0.5$ on the nearest neighbor shell. Thus the overestimation of correlations at X amplifies tendency towards superconductivity, but not towards one specific type. In more general terms, any transfer momentum of the form $q_i = (q, q)$ will generate attraction in the even channel as long as $r q_i > \pi/2$. Below this threshold, the Fourier transformation of $C(q)$ will become positive and thus generate attractive interactions in the odd-channel. Thus also the predicted leading momentum transfer found in DMFT should generate attraction for a singlet state.

To make again a connection to the model at hand, we analyse the attraction induced by a spin-fluctuation vertex for the full 3D model from RPA-flow. We present the attraction values generated by the leading eigenvalues of the interaction at each q in the xy plane, see Fig. 10.

Appendix F: Comparison to 3D results

To ensure that the results from our quasi 2D simulation are applicable to the realistic material, we check for consistency of our results at a few selected points between 2D and 3D calculations. In full 3D calculations more order parameters are allowed to be non zero [63, 70, 71, 73], therefore besides the convergence check of our calculations this is also a consistency check of that the quasi-2D model indeed contains the leading instabilities of the 3D model. For this we simulate a 20^3 grid for the vertex function with an additional refinement of 21^3 for the momentum integration in the loop. First, we estimate the most relevant form-factor contributions. For this, we calculate $C_{o_1, o_3}(q)$ and apply what has been discussed in section E, revealing that the most attractive contributions are the x and y direction nearest bond neighbor bonds as in our 2D simulations and their higher harmonics, see Fig. 10.

Thus, we include the first and second harmonic of this contribution in our calculation - i.e. all neighbors within a distance of 7.8\AA . The $q = 0$ SCOP results for $U = 1.5eV$,

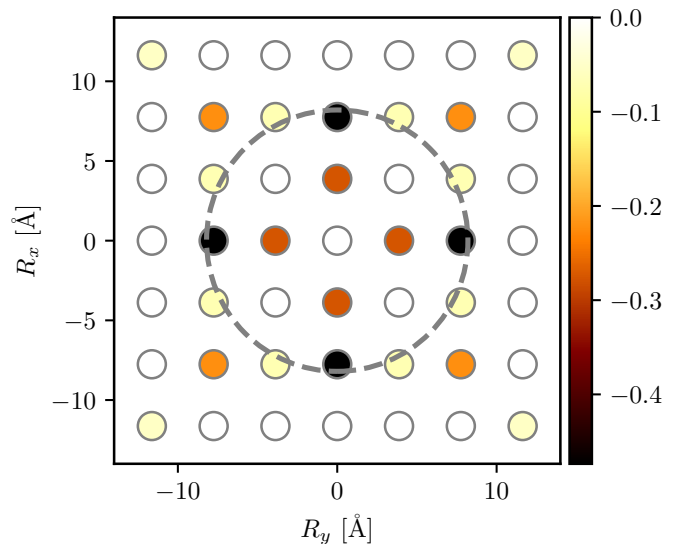


FIG. 10. **Most attractive values of the projection of a spin-spin vertex to the pairing channel in the x - y plane.** For this, we calculate an RPA-like flow for the C -channel up to a scale of $\Lambda = 1e^{-3}$. We plot here the real part of $\Gamma^P(b, b)$ calculated from the dominant eigenvalue of the C channel at each k -point. To incorporate the two leading contributions, we require a form-factor cutoff of 7.8\AA in the full FRG calculation, visually indicated by a circle with radius 8.2\AA to emphasize that the largest attraction value is included.

$J = 0.15U$ and $\epsilon_{xx} = 0.0\%, 0.8\%$ are summarized in Fig. 11.

Our results presented, indicate that the order parameter is indeed purely 2D, thus our 2D simulations capture the main aspects of the real material. Further the critical scale changes slightly from $3.15(3.69)$ meV in 3D to $2.48(2.80)$ meV in 2D with $0.0(0.8)\%$ uniaxial strain applied. Two remarks have to be made: The nearly layered structure gives rise to sub-leading pair-density wave contributions with the same fermionic momentum dependence as presented in Fig. 11 and finite transfer momentum of the form $q = (0, 0, q_z)$. These are however subleading to the $q_z = 0$ SCOP. The existence of these competing pair-density waves can be understood from a simple 2D toy model - assume a two band system which is non-dispersive in one direction:

$$H_{o_1, o_2}(k_x, k_y) = H_{o_1, o_2}(k_x), \quad (\text{F1})$$

this immediately implies that both the particle-hole and particle-particle loop have to be independent of k_y . Thus the spin-spin vertex is of the form

$$V_{o_1, o_2}(k_x, k_y) = V_{o_1, o_2}(k_x) \quad (\text{F2})$$

and the linearized gap equation also being independent of k_y . This implies that in the simple picture, all gaps of the form $\Delta_{o_1, o_2}(k_x, q_y)$ have equal eigenvalue λ independent of q_y explaining why we observe these pair-density waves in the nearly layered system.

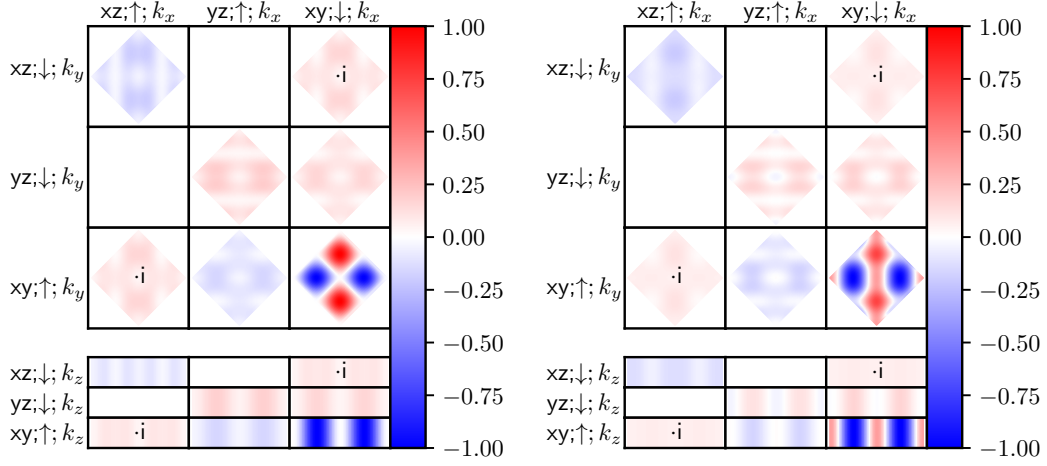


FIG. 11. **2D cuts through the leading eigenvector of the pairing vertex from TUF RG** in $k_x k_y$ (upper panels) and $k_x k_z$ (lower panels) in spin-orbital-momentum representation for the unstrained (left) and 0.8% strained (right) case. We find identical results to our 2D calculation.

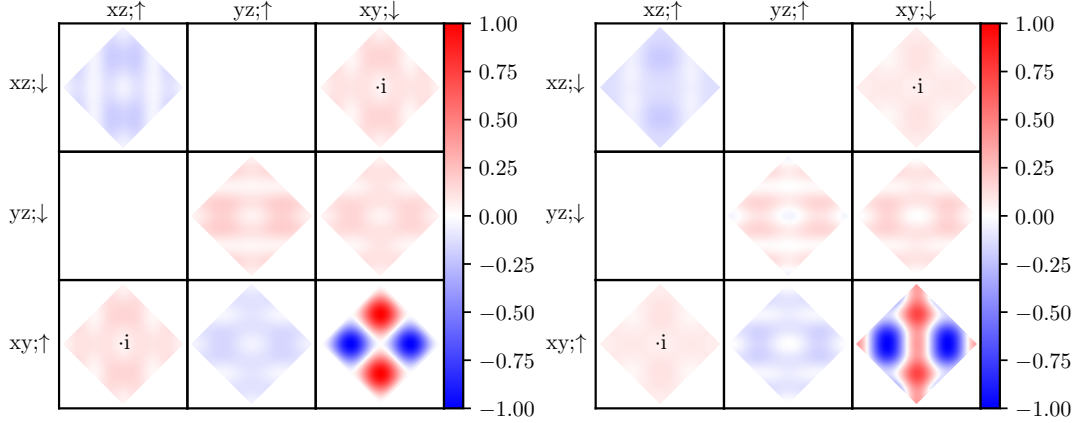


FIG. 12. **Gap functions presented in Fig. 3** calculated on the full BZ, for better comparability with Fig. 11